Field tests of the GeoSTAR Demonstrator Instrument

A.B.Tanner *(Author)*, S.T.Brown, T.C.Gaier, B.H. Lambrigsten
Jet Propulsion Laboratory
California Institute of Technology
Pasadena, USA

B.H. Lim, C.S. Ruf
University Of Michigan
Ann Arbor, USA

F.Torres
Polytechnic University of Catalonia
Barcelona, Spain

Abstract—**Ground based tests of the GeoSTAR (geostationary synthetic thinned array radiometer) demonstrator instrument are reported which simulate the view of the earth from geosynchronous earth orbit (GEO). The test used a 4-meter target disk mounted on a tower above the instrument to simulate the brightness of the earth with a contrasting cold background. Continuous observations at 50.3 GHz for over 100 hours, along with simultaneous atmospheric measurements from independent radiometers, yielded an excellent data set with which to test all aspects of the GeoSTAR calibration. This paper presents a preliminary look at these data, and presents an algorithm to remove the aliased background from the synthesized image.**

Keywords; radiometer; interferometer;

I. INTRODUCTION

GeoSTAR is a synthetic aperture radiometer concept which would for the first time provide high resolution microwave images of the earth from geostationary earth orbit (GEO) in bands from 50 to 183 GHz. The idea is to deploy a Y-array of correlation interferometers, and to use aperture synthesis to achieve high resolution, continuous, hemispheric coverage without any mechanical scanning. In early 2006 a small 24-element, 50-55GHz ground-based demonstration instrument was completed. This instrument provided technical proof that a practical system can meet calibration and performance requirements [1]. Interferometric test data from the antenna range, as well as from solar transit observations provided precise validation of our system at the 0.5% precision level-- which meets mission requirements by analysis. Yet these analysis did not provide any well calibrated test images, and there remained a desire to provide a more compelling demonstration in a relevant environment. In particular, the image synthesis involves a critical de-aliasing step which needs to be demonstrated. The design of GeoSTAR is based on the GEO view of the earth-- which is of a 17 degree diameter disk against a cold, and well modeled cosmic background. This geometry determines the array spacing and antenna diameter, which are both about 3.5 wavelengths. The elemental antenna pattern of our system is approximately Gaussian with a half-power beamwidth of 17 degrees, which matches the earth as well as possible. Yet, inherent to this design, only about half of this antenna pattern energy falls within the earth disk. The remaining half views the cosmic background surrounding the earth, and these regions re-appear as aliases within the central image (as determined by the element spacings). These must be modeled and removed during image synthesis. In space, the cosmic background is readily modeled. For a ground based demonstration the problem is somewhat more difficult. The far-field of the demonstrator instrument is over 200 meters, which would require a target of some 50 meters diameter to represent the earth view from GEO. In the Summer of 2006, we found a suitable solution by re-focusing GeoSTAR to operate in the near field [2]. This permitted operation at 16 meters range with a more practical target disk of about 4 meters diameter. This near field operation induced parallax errors which are mostly corrected with a simple phase correction. We made our observations at the lowest operating frequency of 50.3 GHz so that the atmospheric opacity could be reduced to some 30%, and the sky background temperature of some 100 Kelvin could be modeled.

Figure 1. GeoSTAR test setup. GeoSTAR is the white box to the right, which tilted up by about 39 degrees. The target disk is at a range of 16 meters to the west. The 2x2 and 4x4 heated boxes inside of the disk are visible.

II. TEST CONFIGURATION

Figure 1 shows the test configuration as conducted on the JPL Mesa antenna range facility in the summer of 2006. The target consisted of a light weight, 12 foot (4 meter) diameter disk constructed from foil clad foam insulating sheets, which were lined on the bottom side with microwave absorber material and then covered with 1 cm expanded polystyrene for thermal insulation. In the center of the disk, two similarly constructed boxes where attached which contained convective (circulated air) heaters which raise the temperatures in two zones to about 60 Celsius. One box was 4 x 4 foot (1.2 x 1.2 m) square, and the other was 2 x 2 foot (60 x 60 cm) square. This provided a time-variable contrast within the disk. A noise

diode source was placed in the center of the disk as a phase reference for the near-field correction. The accuracy of the temperature knowledge of the target disk was approximately +/- 1 C in the ambient regions, approximately +/- 2 C within the 2x2 heated target, and approximately +/- 3C within the larger 4x4 target. These estimates are based on thermal gradients which were observed among 24 thermistors distributed within the absorber materials. Errors in the heated targets were caused by difficulties of distributing the heat evenly over a large surface with limited insulation and air circulation.

The background temperature of the sky was estimated with a nearby water vapor radiometer (WVR) operating at 20.7 and 31.4 GHz. The background temperature was extrapolated from this instrument to a precision which was estimated at +/- 3 Kelvin, primarily due to known errors in the WVR. The extrapolation from 20.7 and 31.4 GHz to 50.3 GHz was based on pressure-corrected regression of forward modeled radiances from representative radiosonde data. The zenith-angle 50.3 GHz brightness temperatures, T_z, estimates from the WVR were then mapped to a given elevation angle, θ, using the radiative transfer calculation

$$T(\theta) = T_e - (T_e - 2.7)l_Z^{\frac{1}{\sin(\theta)}}, \text{ with } l_z = \frac{T_e - T_Z}{T_e - 2.7} \quad (1)$$

where l_z is zenith transmissivity, T_e is an effective air temperature of T_e= 285 K, and the quantity $1/\sin(\theta)$ is the airmass along a line of sight. Temperature below the horizon was estimated as a flat 285 K-- which is a poor approximation-- but of little consequence since our radiometer looked upward from the ground.

The calibration of GeoSTAR has thus far been based on observations of a liquid nitrogen (LN2) and ambient targets just prior to the experiment for noise temperature estimates, and on antenna range measurements made several months prior to the experiment for phase alignment. GeoSTAR contains a noise diode which is distributed to the entire array and injected behind the antennas. The deflections of correlators by this noise diode while observing the LN2 and ambient loads were sufficient to estimate the noise diode and receiver noise temperatures throughout the array. The phases of the injected noise diode were also measured on the antenna range relative to a point source at boresight. These numbers were then applied to the noise diode deflections during target observations to scale the complex correlations to visibility. There were many errors at the ~2 % level associated with these calibrations-- primarily related to the thermal stability and humidity control within the instrument, and there are many improvements that we intend to make. The details are beyond the scope of this paper, but it is worth adding that these errors were comparable to other errors in our test.

III. IMAGE SYNTHESIS WITH ALIAS REMOVAL

The aliased regions of the GeoSTAR field of view (FOV) were removed in the visibility domain by subtracting the model of the "background" visibility in the absence of the target disk. Visibility versus antenna element spacing, u and v (with units of radians), were estimated from the modeled brightness image,

T(r,s), and antenna pattern, F(r,s), over the FOV with the forward model of GeoSTAR,

$$V(u,v) = \iint\limits_{2\pi} T(r,s)F(r,s)\exp[-j(ru+sv)]drds \quad (2)$$

where r and s are the horizontal and vertical image coordinates, and the following definitions apply which map the normalized antenna voltage pattern model, f, with associated beam solid angle, Ω, from spherical coordinates (θ,φ) onto the image (r-s) plane:

$$F(r,s) \equiv \frac{|f(\theta,\varphi)|^2}{\Omega\sqrt{1-r^2-s^2}}, \quad \begin{array}{l} r \equiv \sin\theta\cos\varphi \\ s \equiv \sin\theta\sin\varphi \end{array} \quad (3)$$

To date, we have modeled f with a spherical wave expansion of our horn design, which has been validated on the antenna range at the 2% level. The sky brightness temperature of (1) was mapped to a model image, T(r,s) in (2), with a rotation of coordinates to the upward tilt of GeoSTAR-- which was about 40 degrees above the horizon in Figure 1. This model was computed over the entire hemisphere in order to capture all of the antenna energy in the "background" model.

As detailed in references [1], the GeoSTAR demonstrator instrument contains 8 antenna elements in each of 3 arms, which yield 192 ($=3*8^2$) unique complex visibility measurements on a hexagonal sample grid of the U-V aperture plane. There is also a single, real-valued sample at the origin of the U-V plane which represents the total antenna power (i.e. the mean antenna brightness). In practice, all these samples were combined in a real-valued vector of 385 ($=192*2 +1$) linearly independent visibility samples, and the integral of (2) was implemented with the following matrix equation and definitions

$$V = GFT \quad (4)$$

$$V \equiv \begin{bmatrix} V(0,0) \\ Re[V(u_1,v_1)] \\ Im[V(u_1,v_1)] \\ \vdots \\ Im[V(u_{192},v_{192})] \end{bmatrix},$$

$$G \equiv \begin{bmatrix} 1 & \cdots & 1 \\ \cos(u_1r_1+v_1s_1) & \cdots & \cos(u_1r_P+v_1s_P) \\ \sin(u_1r_1+v_1s_1) & \cdots & \sin(u_1r_P+v_1s_P) \\ \vdots & \ddots & \vdots \\ \sin(u_{192}r_1+v_{192}s_1) & \cdots & \sin(u_{192}r_P+v_{192}s_P) \end{bmatrix},$$

$$F \equiv \begin{bmatrix} F(r_1,s_1)drds & & 0 \\ & \ddots & \\ 0 & & F(r_P,s_P)drds \end{bmatrix}, \text{ and } T \equiv \begin{bmatrix} T(r_1,s_1) \\ \vdots \\ T(r_P,s_P) \end{bmatrix}, (5)$$

where the quantity drds represents the area of an image pixel given some regular sample grid on the r-s image plane. In these equations, we refer to the G-matrix [3] as the "flat" G-matrix because it represents the straight Fourier Transform without the elemental antenna pattern-- which is instead carried as the diagonal matrix, F. G, F, and T contain P pixels

distributed over some area of the r-s plane with some sample grid density. The fraction of the antenna energy represented by a given sample grid can be calculated as the sum of elements in F. Our software allowed us to vary both the density and the area of the sample grid. For the purpose of modeling the sky background, we found it necessary to sample the entire 2-pi area of the r-s plane. To perform this calculation with a reasonable number of pixels, P, we also lowered the sample grid density. The smooth sky background within the FOV produced very small visibilities (less than millikelvin in most cases), so the errors associated with the low sample grid density were well constrained.

Image synthesis was next performed on the difference between the measured visibilities, and the above background modeled visibilities with the following inversion: Our system measures the visibility function on a regular hexagonal grid on the U-V plane, with an associated spacing of d (= 3.5 wavelengths). Each visibility sample measures a unique harmonic within a common hexagonal region of area A_u on the image (r-s) plane given by

$$A_u = \frac{2\lambda^2}{d^2 \sqrt{3}} \, .$$ (6)

By truncating the integral of (2) to a singe period (of area A_u) we obtained the image synthesis formula by identity with the Periodic Fourier Series as

$$T(r,s) \cong \frac{V(0,0) + 2 \sum_{i=1}^{192} \frac{Re(V(u_i, v_i))\cos(ru_i + sv_i)}{+ Im(V(u_i, v_i))\sin(ru_i + sv_i)}}{A_u F(r,s)}$$ (7)

which has the matrix form

$$T \cong F'G'V$$ (8)

where the primed terms represent the reciprocal matrices to G and F of (5) as follows

$$G' = \begin{bmatrix} 1 & 2\cos(u_1 r_1 + v_1 s_1) & \cdots & 2\sin(u_{192} r_1 + v_{192} s_1) \\ \vdots & \vdots & \ddots & \vdots \\ 1 & 2\cos(u_1 r_P + v_1 s_P) & \cdots & 2\sin(u_{192} r_P + v_{192} s_P) \end{bmatrix},$$

$$F' = \begin{bmatrix} \frac{1}{A_u F(r_1, s_1)} & & 0 \\ & \ddots & \\ 0 & & \frac{1}{A_u F(r_P, s_P)} \end{bmatrix}$$ (9)

This solution is only valid for sources within the region of area A_u. By subtracting the background visibilities, we effectively truncate the integral of (2) to this area, and synthesize the image of a disk which is surrounded by zero Kelvin. The final step of our algorithm must then add the model of the sky background temperature to this image. The entire image alias removal and synthesis process is summarized with the following equation:

$$T_f \cong F_f' G_f' \left(V_{meas} - G_b F_b T_{b-sky} \right) + T_{f-sky}$$ (10)

where V_{meas} is the vector of measured visibilities, and the subscripts "b" and "f" refer to the different sample grids which

are associated with the full-hemispheric 'background' and truncated 'foreground' regions, respectively. T_{f-sky} and T_{b-sky} are otherwise generated with the same model of (1).

IV. TEST RESULTS

Figure 2 shows an example image produced with (10) while observing the target disk. In Figure 2 we see the round shape of the target on top of the support post, and we see the two heated targets: the 2x2 target to the upper left of center, and the 4x4 target below center. This image is very close to our expectations. There are pronounced 'ripples' within the disk which are predictable effects of synthetic sidelobes and the limb contrast which will be eliminated with further image processing. There are also aliases of the support post below the target which appear in the left and right edges of the hexagonal image area. Note that aliasing follows three axes such that any object which moves past one edge of the hexagonal FOV immediately reappears at the opposing edge. As the object moves further away, the aliased image tends to fade in magnitude with the antenna pattern. The support post happens to be centered below the two diagonal axes, which places the alias along the left and right vertical margins of the hexagon. The alias is strongest at the top of these margins, and fades with the antenna pattern as it descends further down these margins.
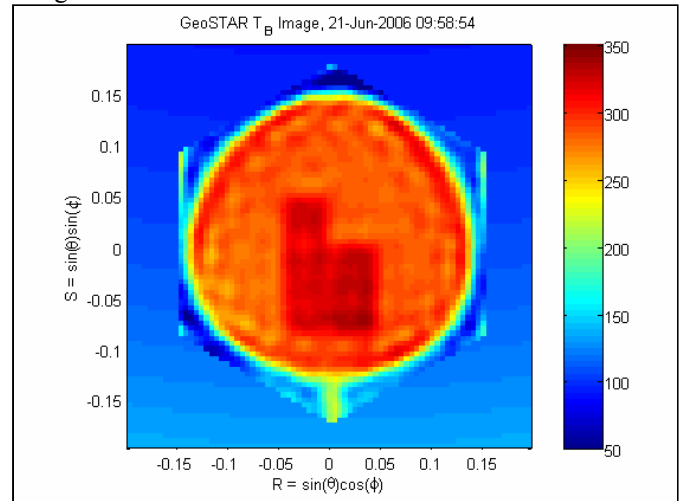

Figure 2. GeoSTAR image of the target disk. The 2x2 and 4x4 heated zones and the support post are visible. Aliased images of the support post appear in the right and left margins of the hexaginal image region.

Figure 3 plots some sample temperatures which have been extracted from three regions within the synthesized image and plotted as a time series as the two heated targets were cycled in temperature. The dashed traces in Figure 3 are the thermistor temperatures within the targets. The three regions represent the 2x2, 4x4, and ambient areas of the target. A spatial average of the thermistors and of the pixels apply in all cases. These results show that the target was indeed quite accurately measured by GeoSTAR. The largest errors of some 5 K in the early part of this example is common to all three temperature zones, and this can be traced to difficulties that we encountered estimating the mean antenna brightness (which has since been corrected).
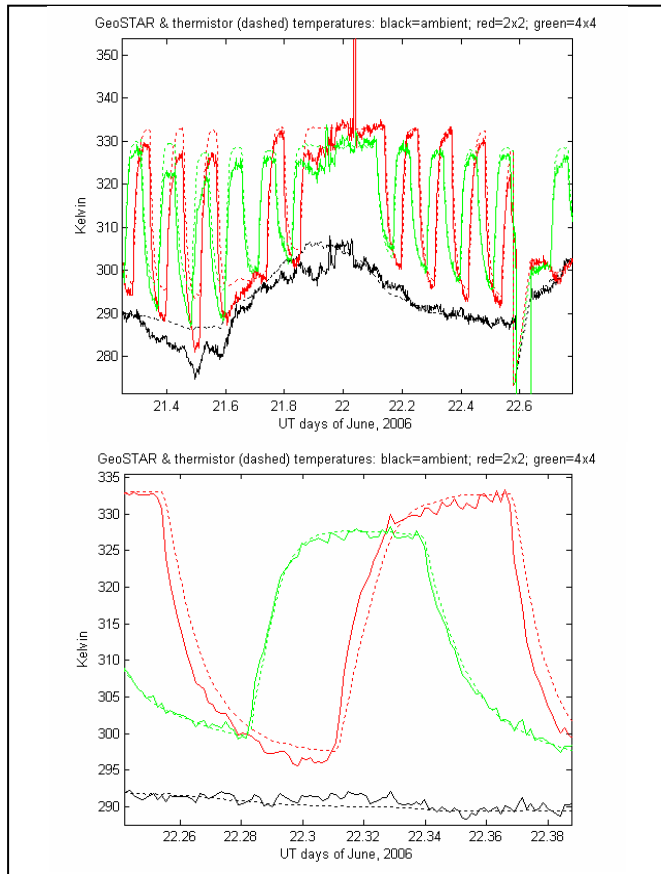
Figure 3. GeoSTAR (solid traces) and thermistor (dashed traces) temperatures of the ambient (black), 2x2 (red) and 4x4 (green) zones of the target.

Figure 4 plots double-differences between the heated-minus-ambient thermistor temperatures and the heated-minus-ambient GeoSTAR measurements of Figure 3. These indicate how well GeoSTAR resolved the contrast between the heated and ambient zones of the target in a manner which is insensitive to the large mean temperature errors that we encountered. The 2x2 target plots show a series of 5 K 'spikes' which can be traced to a time lag in the thermistor measurements of the absorber material. The 2x2 target used a thicker absorber foam which was more difficult to heat or cool rapidly with the circulated air, so the thermistor temperatures within the foam tended to lag behind the microwave temperature. This effect is also evident in the expanded plot of Figure 3. Apart from these transients, we see that the steady state readings are in good agreement at the 1 K level-- which is a very good result when we consider all of the errors which have not yet been corrected.

V. CONCLUSION

A first order model and calibration of GeoSTAR has been demonstrated which shows relative accuracies within the simulated earth disk which are on the order of 1 Kelvin, and absolute errors which are on the order of 5 Kelvin. This is really quite a good result, considering the simplified model which has been applied thus far. The remaining errors are well explained by (1) antenna pattern gain anomalies within the array which were measured previously on the antenna range at the ~2% level; (2) near-field errors at the ~5% level due to offsets of antenna elements in the array; (3) noise temperature calibration errors on the order of 2% due to poorly characterized thermal sensitivities and uncertainties of the thermal and humidity control; (4) phase errors related to the non-ideal geometry of the array and thermal and humidity instabilities of the noise diode distribution network; and (5) uncertainty in the target and background "ground truth" data of some 2 ~ 3 K. With the exception of (5), we anticipate that all of the above errors will be reduced drastically with better system models, and with a revised inversion using the known response.
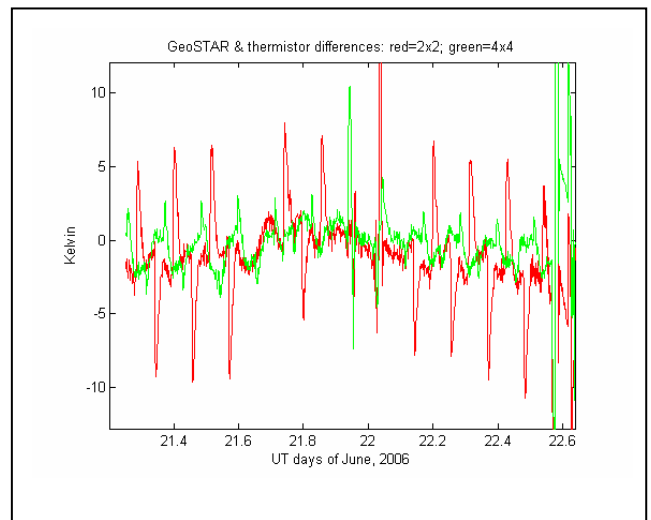

Figure 4. Temperature errors associated with Figure 3, as computed from double differences; e.g. as $(T_{2x2}-T_{amb})_{GeoSTAR}-(T_{2x2}-T_{amb})_{thermistor}$.

REFERENCES

[1] Tanner, A.B., et al., "Initial results of the Geostationary Synthetic Thinned Array Radiometer (GeoSTAR) Demonstrator Instrument," IEEE Trans. Geoscience & Remote Sensing, Special Issue on MicroRad'06, Puerto Rico, publication expected in 2007.

[2] Tanner,A.B., F. Torres, B. H. Lambrigsten, T. M. Gaier, "Near Field characterization of the GeoSTAR demonstrator". Proc IEEE International Geoscience and Remote Sensing Symposium (IGARSS-06). IEEE, 2006, p. - .

[3] Tanner, A.B., and Swift C.T., "Calibration of a Synthetic Aperture Radiometer," IEEE Trans. Geoscience & Remote Sensing, Vol.31, No. 1, Jan. 1993.